



Contents lists available at ScienceDirect

Journal of Power Sources

journal homepage: www.elsevier.com/locate/jpowsour

Potentiometric entropy and *operando* calorimetric measurements reveal fast charging mechanisms in $\text{PNb}_9\text{O}_{25}$

Sun Woong Baek^a, Molleigh B. Preefer^{b,e}, Muna Saber^c, Kuan Zhai^d, Matevž Frajnkovič^a, Yucheng Zhou^a, Bruce S. Dunn^{d,f}, Anton Van der Ven^b, Ram Seshadri^{b,e}, Laurent Pilon^{a,f,g,*}

^a Mechanical and Aerospace Engineering Department, Henry Samueli School of Engineering and Applied Science, University of California, Los Angeles, CA 90095, USA

^b Materials Department, and Materials Research Laboratory, University of California, Santa Barbara, CA 93106, USA

^c Department of Chemical Engineering, University of California, Santa Barbara, CA 93106, USA

^d Materials Science and Engineering, Henry Samueli School of Engineering and Applied Science, University of California, Los Angeles, CA 90095, USA

^e Department of Chemistry and Biochemistry, University of California, Santa Barbara, CA 93106, USA

^f California NanoSystems Institute, University of California, Los Angeles, Los Angeles, CA 90095, USA

^g Institute of the Environment and Sustainability, University of California, Los Angeles, Los Angeles, CA 90095, USA

HIGHLIGHTS

- Entropy data show ion ordering and semiconductor to metal transition in $\text{PNb}_9\text{O}_{25}$.
- Heat generation rates are measured at each electrode under galvanostatic cycling.
- Reversible heat generation is dominated by entropic changes in the electrode.
- Small enthalpy of mixing at high C-rates is a sign of a high cycling rate material.
- Energy balance shows that electrical energy losses are dissipated in the form of heat.

ARTICLE INFO

Keywords:

Lithium ion battery
 $\text{PNb}_9\text{O}_{25}$ anode
 Entropy measurements
 semiconductor-to-metal transition
 Calorimetry

ABSTRACT

The Wadsley–Roth compound $\text{PNb}_9\text{O}_{25}$ is a promising fast charging lithium ion battery anode material with high operating voltage to prevent solid electrolyte interface formation. Here, we present potentiometric entropy measurements featuring signatures of semiconductor-to-metal transition and intralayer ordering upon lithiation in the anode material $\text{PNb}_9\text{O}_{25}$ that could not be observed with *in situ* X-ray diffraction. In addition, the instantaneous heat generation rates at the $\text{PNb}_9\text{O}_{25}$ working electrode and at the lithium metal counter electrode during galvanostatic cycling were measured individually for the first time by *operando* isothermal calorimetry. The heat generation rate decreased at the $\text{PNb}_9\text{O}_{25}$ electrode upon lithiation due to the decrease in electrical resistivity caused by the semiconductor-to-metal transition observed in potentiometric entropy measurements. Furthermore, the heat generation rate at the lithium metal electrode was positive during delithiation due to the exothermic plating of Li^+ ions on the lithium metal counter electrode associated with dendrite formation. Furthermore, calorimetric measurements established that the entropy change dominated the reversible heat generation rate at each electrode. Finally, the contribution of enthalpy of mixing was relatively small even at high C-rates thanks to the high Li^+ ion mobility in $\text{PNb}_9\text{O}_{25}$ confirming its promises as a fast charging anode material.

1. Introduction

Fast charging batteries have been widely studied due to the increase in demand for electric vehicles (EV) and portable electronic devices [1–3]. In particular, lithium-ion batteries (LIBs) feature high energy

density and high power capabilities [4]. However, most of the commercial LIBs use graphite anode and suffer from performance degradation over time due to the formation of solid–electrolyte interface (SEI) layer at the electrode surface [5]. In order to avoid SEI formation, many

* Corresponding author at: Mechanical and Aerospace Engineering Department, Henry Samueli School of Engineering and Applied Science, University of California, Los Angeles, CA 90095, USA.

E-mail address: pilon@seas.ucla.edu (L. Pilon).

<https://doi.org/10.1016/j.jpowsour.2021.230776>

Received 3 September 2021; Received in revised form 2 November 2021; Accepted 12 November 2021

Available online 11 December 2021

0378-7753/© 2021 Elsevier B.V. All rights reserved.

oxide materials featuring high operating voltage (above 1 V versus Li/Li⁺), have been considered as promising LIB anode materials [6,7]. In particular, Wadsley–Roth shear phase based niobium oxides, such as Nb₁₂WO₃₃ [8] and TiNb₂O₇ [9], present the advantage of high operating voltage, structural stability, cycle reversibility, and high energy density. In addition, a combination of edge-shared and corner-shared octahedra in this type of shear crystal structure forms many open-tunnel-like regions where Li⁺ ions can rapidly diffuse during lithiation and delithiation [10,11].

Among materials with Wadsley–Roth crystallographic shear structure, PNB₉O₂₅ is a promising fast charging anode material for its ability to engage in multielectron redox reactions resulting in high specific capacity [12,13]. In addition, it features two voltage plateaus above 1.0 V (versus Li/Li⁺), thus avoiding SEI formation [14,15]. Furthermore, PNB₉O₂₅ undergoes an insulator-to-metal transition, which is highly favorable for fast cycling battery applications when transition metals are required to transport electron rapidly [12]. Unfortunately, such transition cannot be observed in conventional characterization techniques such as X-ray diffraction (XRD) [12]. Therefore, alternative characterization techniques are desirable to further identify and understand such phenomena taking place in battery electrodes during cycling. In fact, thermodynamic measurements can unravel the origins of physicochemical phenomena occurring in batteries [16,17]. In LIB cells, the open circuit voltage $U_{ocv}(x, T)$ is directly related to the change in the Gibbs free energy of reaction of the system [18]. In addition, the derivative of $U_{ocv}(x, T)$ with respect to temperature T for a given lithium composition x , $\partial U_{ocv}(x, T)/\partial T$, also known as the entropic potential, can be used to estimate the partial molar entropy of the cell [17,19]. The entropic potential measurement is particularly insightful for understanding the structural stability upon phase transitions in the electrode material [17]. In addition, our recent *operando* calorimetry can directly measure the instantaneous heat generation rate in each electrode of a battery cell during charging/discharging [20]. The measurements can enable a complete energy balance of the cell and can provide insights into the different phenomena contributing to energy dissipation upon charging/discharging including resistive losses, enthalpy of mixing, and reversible entropic processes [19].

The present study aims to identify the entropic and calorimetric signatures of the different physicochemical phenomena taking place during charging/discharging at the PNB₉O₂₅ working electrode and at the lithium metal counter electrode. Potentiometric entropy and calorimetry measurements were combined with XRD measurements to understand the structural changes in the PNB₉O₂₅ upon lithiation/delithiation. Furthermore, the instantaneous heat generation rate measurements at each electrodes during cycling was used to deepen our understanding into electrochemical phenomena resulting in heat dissipation.

2. Background

2.1. Potentiometric entropy measurements

Potentiometric entropy measurement is a technique measuring the entropic potential $\partial U_{ocv}(x, T)/\partial T$ for a given lithium composition x . The open circuit voltage $U_{ocv}(x, T)$ of the battery cell with a PNB₉O₂₅-based working electrode and a lithium metal counter electrode can be defined from the Nernst equation as [18]

$$U_{ocv}(x, T) = -\frac{\mu_{Li}^{PNO}(x, T) - \mu_{Li}^o(T)}{e}. \quad (1)$$

Here, e is the unit charge and $\mu_{Li}^{PNO}(x, T)$ and $\mu_{Li}^o(T)$ are respectively Li chemical potentials in the PNB₉O₂₅-based working electrode and lithium metal counter electrode. In addition, the composition x is defined as the fraction of the number of intercalated lithium N_{Li} per number of PNB₉O₂₅ units N_{PNO} , i.e., $x = N_{Li}/N_{PNO}$. The chemical

potential $\mu_{Li}^{PNO}(x, T)$ of Li within the PNB₉O₂₅ electrode is related to the Gibbs free energy of the PNB₉O₂₅ compound according to [18]

$$\begin{aligned} \mu_{Li}^{PNO}(x, T) &= \frac{\partial G_{PNO}(x, T)}{\partial N_{Li}} = \left(\frac{\partial g_{PNO}(x, T) N_{PNO}}{\partial x} \right) \left(\frac{\partial x}{\partial N_{Li}} \right) \\ &= \frac{\partial g_{PNO}(x, T)}{\partial x} \end{aligned} \quad (2)$$

where $g_{PNO}(x, T)$ is the Gibbs free energy of PNB₉O₂₅ normalized by the number N_{PNO} of PNB₉O₂₅ units. Furthermore, the chemical potential $\mu_{Li}^o(T)$ of Li in the lithium metal counter electrode can be expressed as

$$\mu_{Li}^o(T) = \frac{\partial G_{Li}}{\partial N_{Li}} = \frac{G_{Li}}{N_{Li}} = g_{Li}^o(T) \quad (3)$$

where the middle equality holds because the counter electrode is a single component solid of pure Li metal. Here, Eq. (3) considers that the Li metal electrode with macroscopic dimensions so that contributions from surface energy can be neglected. In this thermodynamic limit, the Li chemical potential of the anode is a constant when holding the temperature and pressure constant. By substituting Eqs. (2) and (3) into Eq. (1), the open circuit voltage $U_{ocv}(x, T)$ can be expressed as

$$U_{ocv}(x, T) = -\frac{1}{e} \left[\frac{\partial g_{PNO}(x, T)}{\partial x} - g_{Li}^o(T) \right]. \quad (4)$$

Based on the Clairaut's theorem, taking the derivative of both sides of Eq. (4) with respect to temperature T yields

$$\frac{\partial U_{ocv}(x, T)}{\partial T} = -\frac{1}{e} \left[\frac{\partial}{\partial x} \left(\frac{\partial g_{PNO}(x, T)}{\partial T} \right) + \frac{\partial g_{Li}^o(T)}{\partial T} \right]. \quad (5)$$

The temperature derivative of the molar Gibbs free energy under isobaric conditions is related to the entropy $s(T)$ according to Maxwell's relations as [21]

$$s(x, T) = -\frac{\partial g(x, T)}{\partial T}. \quad (6)$$

where both $s(x, T)$ and $g(x, T)$ are normalized quantities per mole of PNB₉O₂₅ or metallic Li. Thus, it is possible to relate the temperature derivative of the open circuit voltage to the entropies of the PNB₉O₂₅ and lithium metal electrodes according to

$$\frac{\partial U_{ocv}(x, T)}{\partial T} = \frac{1}{e} \left[\frac{\partial s_{PNO}(x, T)}{\partial x} - s_{Li}^o(T) \right]. \quad (7)$$

Therefore, the measured $\partial U_{ocv}(x, T)/\partial T$ depends on the partial molar entropy of PNB₉O₂₅, denoted by $\partial s_{PNO}(x, T)/\partial x$, since s_{Li}^o is independent of x . Thus, analyzing $\partial U_{ocv}(x, T)/\partial T$ measurements can provide insights in the physicochemical phenomena occurring in the PNB₉O₂₅ working electrode.

2.2. Heat generation in batteries

The total heat generation rate $\dot{Q}_T(x, T)$ (in W) in a battery can be attributed to four main phenomena including (i) Joule heating $\dot{Q}_J(x, T)$, (ii) reversible entropic heat generation $\dot{Q}_{rev}(x, T)$, (iii) enthalpy of mixing $\dot{Q}_{mix}(x, T)$, and (iv) undesirable side reactions $\dot{Q}_{sr}(x, T)$. Thus, $\dot{Q}_T(x, T)$ can be expressed as [19,22–24],

$$\dot{Q}_T(x, T) = \dot{Q}_J(x, T) + \dot{Q}_{rev}(x, T) + \dot{Q}_{mix}(x, T) + \dot{Q}_{sr}(x, T) \quad (8)$$

where $\dot{Q}_T(x, T)$ is positive when the cell releases thermal energy and negative when it absorbs heat.

Assuming uniform temperature and constant volume, the exothermic Joule heating $\dot{Q}_J(x, T)$ owing to irreversible resistive losses caused by the deviation of the cell operating voltage $V(x, T)$ from its equilibrium potential can be expressed as [19,22–24],

$$\dot{Q}_J(x, T) = I[V(x, T) - U^{avg}(x, T)]. \quad (9)$$

Here, I is the applied current and $U^{avg}(x, T)$ is the open circuit voltage evaluated at the volume-average concentration in the cell considering

a single electrochemical reaction [25]. In other words, $U^{avg}(x, T)$ is “the potential to which the cell would relax if the current were interrupted [24]”. In practice, $U^{avg}(x, T)$ can be measured using GITT at the same C-rate as that used for the calorimetric measurements. The difference $[V(x, T) - U^{avg}(x, T)]$ is the so-called battery overpotential. In LIBs, the overpotential corresponding to the voltage drop due to internal resistance. As such, the overpotential increases with increasing charge-transfer resistance [26], decreasing ionic conductivity [26], increasing electrolyte viscosity [27] and degradation upon cycling [28,29].

The reversible entropic heat generation rate $\dot{Q}_{rev}(x, T)$ due to changes in the entropy of the device upon lithiation/delithiation can be written as [22–24]

$$\dot{Q}_{rev}(x, T) = IT \frac{\partial U^{avg}(x, T)}{\partial T}. \quad (10)$$

While the irreversible heat generation is related to concentration polarization, activation polarization, and ohmic polarization, the reversible heat generation is related to the chemical reactions occurring in the cell [30]. In the limiting case of charging near equilibrium conditions (i.e., under extremely small currents), Li would be uniformly distributed within the cell and the potentials would be such that $V(x, T) = U^{avg}(x, T) = U_{ocv}(x, T)$. Then, $\dot{Q}_J(x, T) \sim 0$ and heat generation would be solely due to $\dot{Q}_{rev}(x, T)$ [31]. However, under high C-rates, $\dot{Q}_J(x, T)$ dominates [31] and Li concentration gradients form within the electrode due to diffusion limitation. The latter results in additional irreversible heat generation due to enthalpy of mixing [19, 22–24], as discussed later.

The enthalpy of mixing $\dot{Q}_{mix}(x, T)$ associated with ion concentration gradients caused by mass transfer resistance in the LIB can be expressed as [22–24]

$$\dot{Q}_{mix}(x, T) = - \int_{V_{\infty}} \sum_i [\bar{h}_i(x, T) - \bar{h}_i^{avg}(x, T)] \frac{\partial c_i}{\partial t} dV \quad (11)$$

where V_{∞} is the volume of the cell, $\bar{h}_i(x, T)$ is the partial molar enthalpy of species i and the superscript “avg” refers to the partial molar enthalpy corresponding to the volume-averaged concentration, and c_i is the local concentration of species i . For LIBs, the enthalpy of mixing can be further divided into four different contributions associated with ionic concentration gradients (i) across the electrolyte due to mass transfer, (ii) across the electrode due to non-uniform current distribution, (iii) within vacancies, and (iv) within intercalated lithium ions in the electrode due to electrochemical reactions [25,32]. In general, the concentration gradient of the intercalated lithium ions represents the largest contribution to the enthalpy of mixing of the electrode [24]. Conceptually, $\dot{Q}_{mix}(x, T)$ should vanish if Li^+ ion transport is infinitely fast.

Lastly, the heat generation due to undesirable side reactions $\dot{Q}_{sr}(x, T)$ can be written as [22–24]

$$\dot{Q}_{sr}(x, T) = - \sum_i \Delta H_i \dot{r}_i(t). \quad (12)$$

Here, ΔH_i is the enthalpy of reaction of chemical reaction i occurring at reaction rate $\dot{r}_i(t)$. Note that most studies on heat generation in LIBs have neglected $\dot{Q}_{sr}(x, T)$ [22–24]. In fact, the side reactions are avoided by operating the device in an appropriate potential range [33]. Also, the aging process of LIBs takes place at relatively slow rates [22]. Thus, the magnitude of $\dot{Q}_{sr}(x, T)$ is much smaller than that of $\dot{Q}_J(x, T)$, $\dot{Q}_{rev}(x, T)$, and $\dot{Q}_{mix}(x, T)$ under normal operation [23].

2.3. Energy balance

The total thermal energy Q_T (in J) released during a cycle as well as the irreversible heat dissipated in the form of Joule heating Q_J and enthalpy of mixing Q_{mix} can be expressed as [23]

$$Q_i = \oint_{cycle} \dot{Q}_i(x, T) dt \quad \text{with } i = T, J, rev \text{ or } mix \quad (13)$$

By definition, integrating the reversible heat generation rate $\dot{Q}_{rev}(x, T)$ with respect to time over an entire cycle should vanish, i.e., $Q_{rev}=0$.

On the other hand, the net electrical energy losses ΔE_e (in J) corresponds to the difference between the electrical energy provided during charging and that recovered during discharging and is illustrated by the hysteric voltage $V(x, T)$ profile [19,23]. Thus, ΔE_e is expressed as [23]

$$\Delta E_e = \oint_{cycle} V(x, T) dq = \oint_{cycle} V(x, T) I dt \quad (14)$$

where q is the charge transferred upon electrochemical reaction so that $I=dq/dt$. Thermodynamically, the total thermal energy Q_T dissipated during a full cycle should be equal to ΔE_e , i.e., $\Delta E_e = Q_J + Q_{mix} = Q_T$ [19].

2.4. Calorimetry measurements

Many calorimetric measurement techniques, such as accelerating rate calorimetry [34,35], differential scanning calorimetry [36,37], and isothermal calorimetry [19,23] have been used to investigate heat generation in batteries. These calorimetric measurements were used not only to develop a battery thermal management system to avoid thermal runaway [35] but also to understand chemical reactions and transport processes taking place [19,23]. Out of these calorimetric techniques, isothermal calorimetry was particularly insightful to reveal the heat generation associated with electrical energy losses [19,23]. Isothermal calorimetric measurements have been performed during galvanostatic cycling on coin cells [23,36], cylindrical cells [38], swagelok cells [37], and prismatic cells [35]. However, due to the thermal mass of the cells' casings, these calorimetric measurements were performed under low C-rates to maintain the accuracy of the measurements. In order to address this issue, an isothermal calorimeter capable of directly measuring the instantaneous heat generation rate at each electrode has been developed and demonstrated with electric double layer capacitors with activated carbon electrodes in aqueous electrolytes [20], organic electrolytes [39,40], and ionic liquids [41,42] as well as with hybrid pseudocapacitors [43] and battery [19]. By measuring the heat generation rate at individual electrodes, this device can reveal the thermal signatures associated with various physicochemical phenomena including resistive losses [19,40,42–44], ion adsorption/desorption [40,42–44], electrolyte decomposition [41,44], overscreening effect [39,41], and insulator to metal transition [19].

The present study aims to gain insights into the thermodynamic behavior as well as the electrochemical and transport phenomena occurring in $\text{PNb}_9\text{O}_{25}$ anode during cycling. To do so, *operando* potentiometric entropy and isothermal calorimetric measurements were performed on LIB cells consisting of a $\text{PNb}_9\text{O}_{25}$ working electrode and a lithium metal counter electrode in 1M of LiPF_6 in 1:1 v/v EC:DMC electrolyte. Particular attention was paid to entropic change due to phase transitions as well as irreversible and reversible heat generation rates attributed to Joule heating, enthalpy of mixing, and other interfacial and transport processes. The results can also be used to develop thermal management strategies for fast charging battery systems.

3. Materials and methods

3.1. Synthesis of $\text{PNb}_9\text{O}_{25}$ powder

Stoichiometric ratios of Nb_2O_5 (Materion, 99.95%) and $(\text{NH}_4)_3\text{PO}_4$ (Sigma Aldrich, 98%) were ground using an agate mortar and pestle for 20 min to achieve a well-ground mixture. Then, 3 grams of powder was pressed into a 13 mm diameter pellet under 2 tons of force. The pellet was placed into an alumina crucible on a bed of sacrificial powder mixture and heated in air in two steps. First, the material was heated to 623 K for 20 h. Second, the temperature was increased to 1523 K for 18 h and the samples were slowly cooled to room temperature. The average particle size of the synthesized $\text{PNb}_9\text{O}_{25}$ powder was 5 μm and decreased to 1 μm after 30 min of ball-milling.

3.2. Electrode and device fabrication

The synthesized $\text{PNb}_9\text{O}_{25}$ pellet was ground with SuperP (TIMCAL) using an agate mortar and pestle for 5 min until visibly combined. The mixture was transferred to a stainless-steel ball mill canister (5 mL, one ball), and mechanically milled for a total of 20 min in order to achieve thorough mixture of the carbon and active materials. A slurry was prepared by first suspending polyvinylidene fluoride (PVDF) in N-Methyl-2-pyrrolidone (NMP) and speedmixing at 2000 rpm for 10 min. The $\text{PNb}_9\text{O}_{25}$ /carbon mixture was added to the PVDF and speedmixed at 2000 rpm for another 10 min. The resulting slurry had mass ratio 1:0.15:0.05 of $\text{PNb}_9\text{O}_{25}$:conductive carbon:binder. A doctor blade was used to cast the slurry onto a copper foil current collector. The resulting 200 μm thick film was dried at 90 °C under vacuum for 18 h. Then, electrodes were punched into a 10 mm diameter disc. The mass loading of active material on the electrode was 6.2 mg/cm^2 .

Cyclic voltammetry and galvanostatic cycling were conducted using a coin cell configuration (MTI parts, 2032 SS casings). All coin cells were fabricated in an Ar-filled glove box and consisted of a 200 μm thick $\text{PNb}_9\text{O}_{25}$ electrode with 1 M of LiPF_6 in EC:DMC 1:1 v/v (Sigma Aldrich) as the electrolyte, a $10 \times 10 \times 1$ mm thick polished metallic lithium (Sigma Aldrich) ribbon as the counter electrode, and a 200 μm thick glass microfiber filter separator (Whatman, Grade GF/C). The coin cells were cycled using a high accuracy potentiostat (Biologic, VSP-300) in the voltage range of 1.0–3.0 V.

3.3. Material characterization

In order to confirm the formation of the desired composition and phase, X-ray diffraction spectra were collected using a Panalytical Empyrean powder diffractometer equipped with Cu K- α radiation ($\lambda = 1.5406 \text{ \AA}$). The $\text{PNb}_9\text{O}_{25}$ powder was distributed onto a Si zero-background plate and the data were collected in Bragg–Brentano geometry. Rietveld refinement was performed using TOPAS (Academic v.6) and fit to the previously solved space group for $\text{PNb}_9\text{O}_{25}$ $I4/m$ [15].

3.4. Potentiometric entropy measurements

The open circuit voltage $U_{ocv}(x, T)$ and the entropic potential $\partial U_{ocv}(x, T)/\partial T$ of the coin cells with the $\text{PNb}_9\text{O}_{25}$ anode and lithium metal counter electrode were measured as functions of lithium composition x with a potentiometric entropy measurement technique using the apparatus described previously [19] and in supplementary material. The potentiometric entropy measurements procedure consists of imposing a series of constant current pulses each followed by a relaxation period. Here, the constant current pulse lasted 30 min with a current of 130 μA corresponding to a C-rate of C/10. After each current pulse, the cells were allowed to relax for 90 min. During the relaxation period, the temperature of the coin cell was varied from 15 °C to 25 °C in 5 °C increments by imposing a step-like temperature profile using a thermoelectric cold plate (TE technology, CP-121). The temporal evaluation of the cell voltage was recorded with a high accuracy potentiostat (Biologic, VSP-300). Likewise, $U^{avg}(x, T)$ and $\partial U^{avg}(x, T)/\partial T$ were measured using the same procedure as that used for measuring $U_{ocv}(x, T)$, including the same relaxation time, but at different C-rates. The duration of the current pulses also changed with C-rates. For instance, at C-rate of 1C, each current pulse lasted 3 min, while it lasted 2 min for C-rate of 2C, and 1 min for 3C. Before imposing the next temperature step and recording $U_{ocv}(x, T)$ or $U^{avg}(x, T)$, two conditions needed to be satisfied to ensure that the cell had reached thermodynamic equilibrium namely (i) the temperature difference between the cold plate and the top of the coin cell was less than 0.1 °C, and (ii) the time rate of change of the open circuit voltage $\partial U_{ocv}(x, T)/\partial t$ or $\partial U^{avg}(x, T)/\partial t$ was less than 1 mV/h.

3.5. Operando isothermal calorimetry

The instantaneous heat generation rates at the $\text{PNb}_9\text{O}_{25}$ and lithium metal electrodes were measured separately under galvanostatic cycling using a custom-made isothermal calorimeter described previously [20]. Similar to the coin cell assembly, the calorimetric cell consisted of (i) a $1 \times 1 \text{ cm}^2$ square shaped $\text{PNb}_9\text{O}_{25}$ electrode, (ii) two 50 μm thick Celgard C380 polypropylene/polyethylene separator sheets, (iii) 1 M LiPF_6 in EC:DMC 1:1 v/v (Sigma Aldrich) as the electrolyte, and (iv) polished metallic lithium (Sigma Aldrich) as the counter electrode.

Based on the thermal analysis of a single electrode described in Supplementary Materials of Ref. [20], the heat generation rate $\dot{Q}_i(t)$ (in mW) at each electrode was equal to the heat transfer rate $q_i''(t)$ passing through the $1 \times 1 \text{ cm}^2$ thermoelectric heat flux sensor (greenTEG, gSKIN-XP) placed in thermal contact with the back of each electrode such that [20],

$$\dot{Q}_i(t) = q_i''(t)A_i = \frac{\Delta V_i(t)}{S_i} A_i \quad \text{with } i = PNO \text{ or } Li. \quad (15)$$

Here, ΔV_i is the voltage difference measured in each heat flux sensor, A_i denotes the footprint area of the electrode (in cm^2), and S_i is the temperature-dependent sensitivity of the heat flux sensor provided by the manufacturer (in $\mu\text{V}/(\text{W}/\text{cm}^2)$). The total instantaneous heat generation rate in the entire cell can be expressed as the sum of the heat generation rate measured at each electrode, i.e., $\dot{Q}_T(t) = \dot{Q}_{Li}(t) + \dot{Q}_{PNO}(t)$.

Moreover, the instantaneous heat generation rate $\dot{Q}_i(t)$ at electrode “i” can be divided into an irreversible $\dot{Q}_{irr,i}(t)$, and a reversible $\dot{Q}_{rev,i}(t)$ heat generation rate so that $\dot{Q}_i(t) = \dot{Q}_{irr,i}(t) + \dot{Q}_{rev,i}(t)$. Obtaining $\dot{Q}_{irr,i}(t)$ for a battery electrode is rendered difficult by the fact that the electrical conductivity of the electrode may change upon lithiation/delithiation. However, it is convenient to note that, time-averaging $\dot{Q}_{rev,i}(t)$ at each electrode over an entire cycle should yield zero. Thus, the time-averaged irreversible heat generation rate $\bar{\dot{Q}}_{irr,i}(t)$ at electrode “i” can be expressed as

$$\bar{\dot{Q}}_{irr,i} = \frac{1}{t_c + t_d} \int_{\text{cycle}} \dot{Q}_i(t) dt \quad \text{with } i = PNO \text{ or } Li \quad (16)$$

where t_c and t_d are the duration of the charging (delithiation), and the discharging (lithiation) steps, respectively. The time-averaged heat generation rates during either the lithiation (subscript ‘d’) or the delithiation (subscript ‘c’) step can also be calculated as

$$\bar{\dot{Q}}_{i,j} = \frac{1}{t_j} \int_0^{t_j} \dot{Q}_i(t) dt \quad \text{with } i = PNO \text{ or } Li \quad \text{and } j = c \text{ or } d. \quad (17)$$

Thus, the time-averaged reversible heat generation rate during charging or discharging is given by

$$\bar{\dot{Q}}_{rev,i} = \bar{\dot{Q}}_{i,j} - \bar{\dot{Q}}_{irr,i} \quad \text{with } i = PNO \text{ or } Li \quad \text{and } j = c \text{ or } d. \quad (18)$$

Furthermore, under galvanostatic cycling, the time t (in sec) can be converted into the lithium composition x in $\text{Li}_x\text{PNb}_9\text{O}_{25}$ such that

$$x = \frac{It}{3600MC_{theo}}. \quad (19)$$

Here, M is the mass loading of the active material and C_{theo} is the theoretical capacity of $\text{PNb}_9\text{O}_{25}$ estimated as $C_{theo} = 190.3 \text{ mAh/g}$ based on one electron per transition metal.

4. Results and discussion

4.1. Material and electrochemical characterization

Fig. 1(a) shows the XRD pattern of the pristine $\text{PNb}_9\text{O}_{25}$ particles synthesized in this study. The lattice parameters and the atomic positions were refined. Here, the weighted profile R-factor R_{wp} was 18.736, which was slightly high because the peak shape asymmetry was captured. However, all peaks observed in the pattern were assigned to

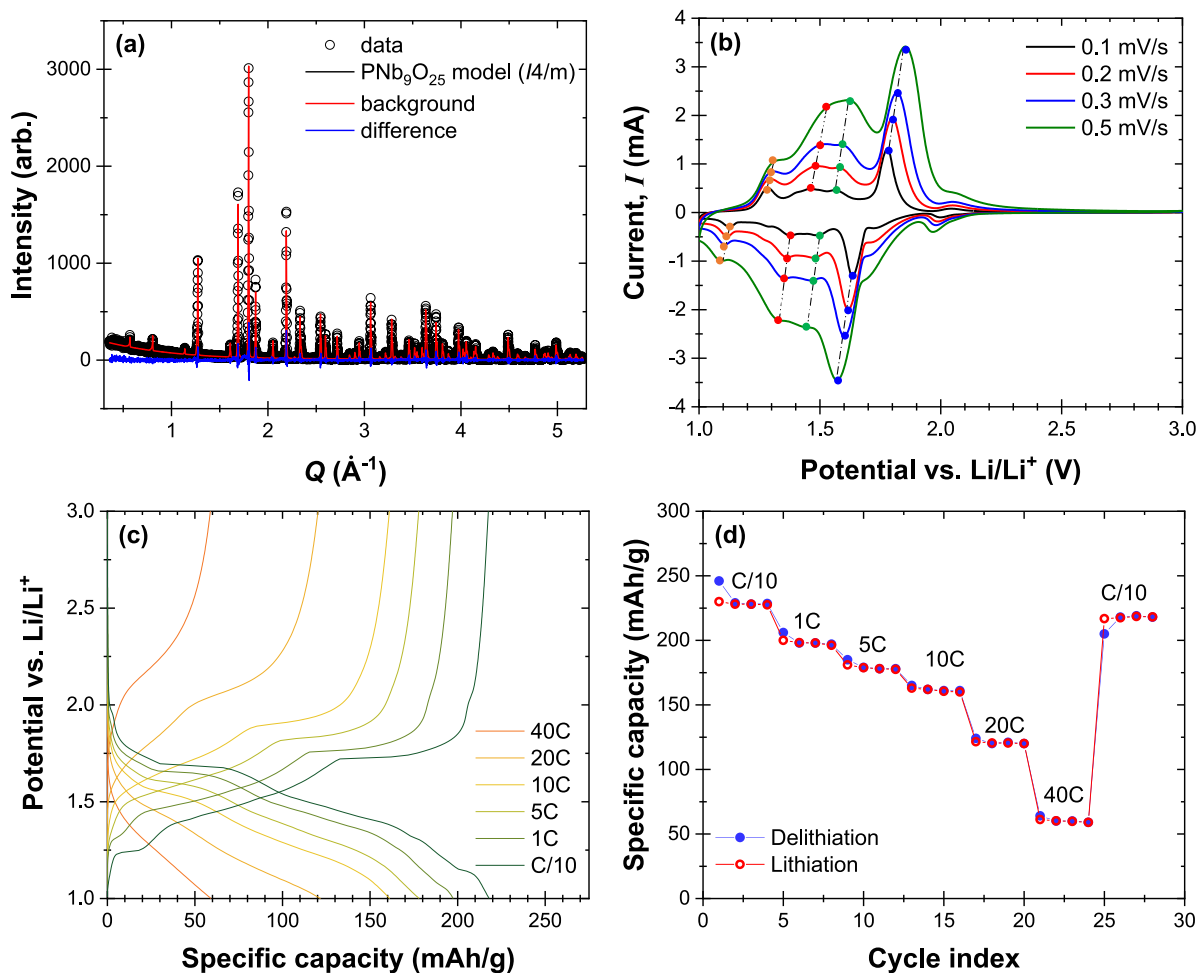


Fig. 1. (a) X-ray diffraction pattern of the pristine $\text{PNb}_9\text{O}_{25}$ particles synthesized, (b) cyclic voltammogram of $\text{PNb}_9\text{O}_{25}$ half-cell cycled with potential window ranging from 1.0 to 3.0 V vs. Li/Li^+ at different scan rates ν , (c) galvanostatic charge-discharge potential profile, and (d) specific capacity retention of the $\text{PNb}_9\text{O}_{25}$ half-cell cycled between 1.0 and 3.0 V vs. Li/Li^+ at C-rates between C/10 and 40C.

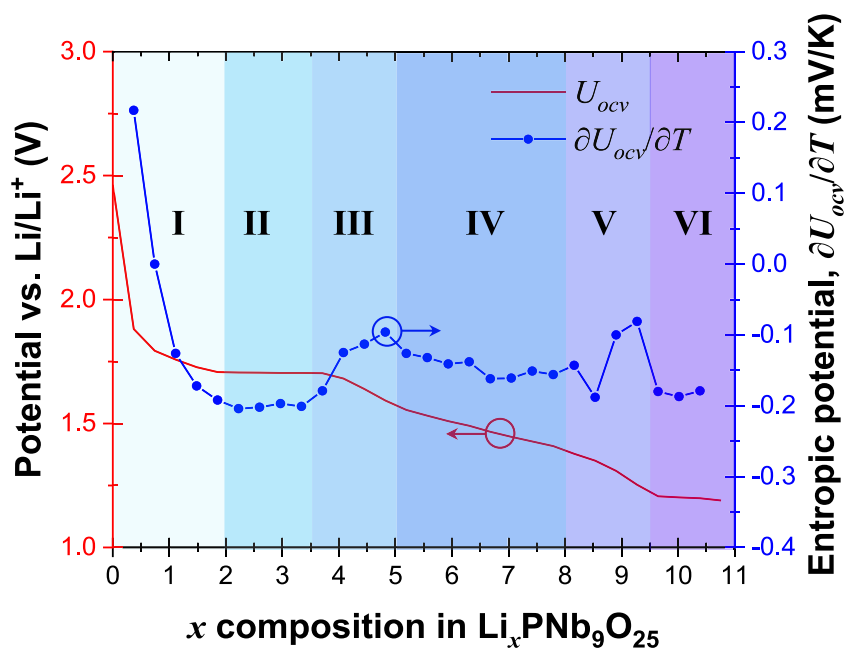


Fig. 2. Open circuit voltage $U_{ocv}(x, T)$ and entropic potential $\partial U_{ocv}(x, T)/\partial T$ of $\text{PNb}_9\text{O}_{25}$ half cell as functions of lithium composition x in $\text{Li}_x\text{PNb}_9\text{O}_{25}$ during lithiation at C-rate of C/10.

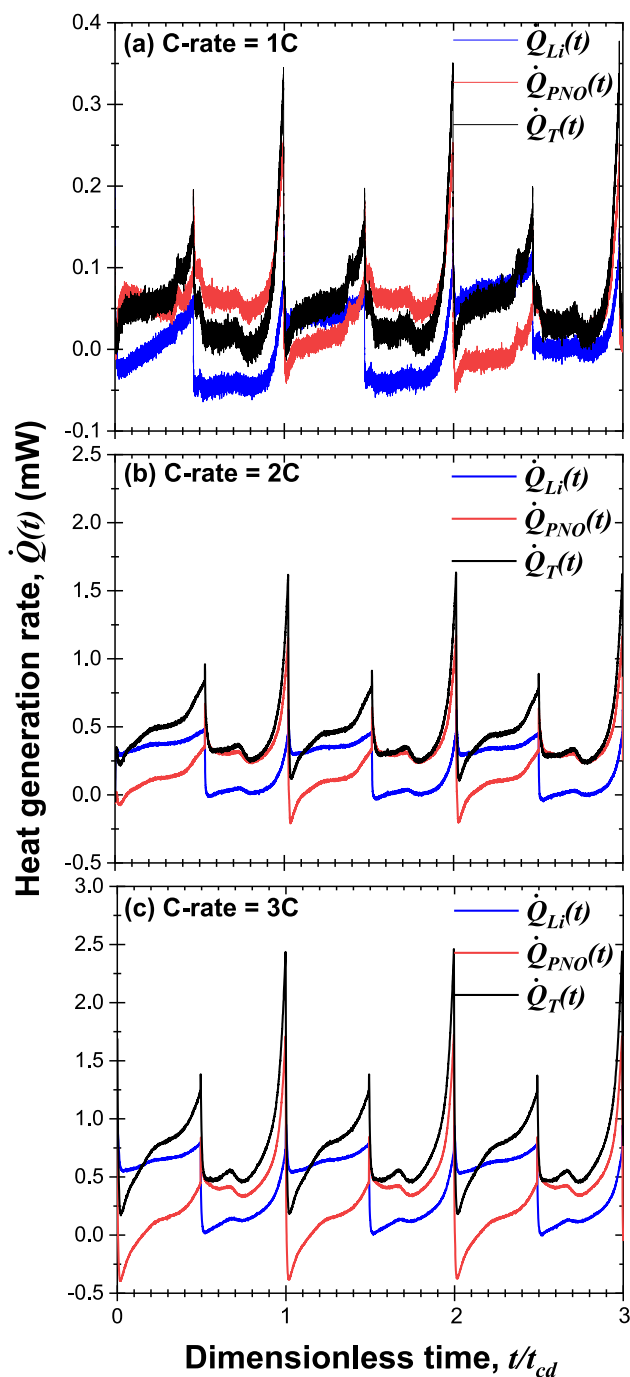


Fig. 3. Measured instantaneous heat generation rates $\dot{Q}_{PNO}(t)$ at the $\text{PNb}_9\text{O}_{25}$ electrode, $\dot{Q}_{Li}(t)$ at the lithium metal electrode, and $\dot{Q}_T(t) = \dot{Q}_{PNO}(t) + \dot{Q}_{Li}(t)$ in the cell as functions of dimensionless time t/t_{cd} for three consecutive cycles with potential window ranging from 1.0 V to 3.0 V vs Li/Li^+ at C-rates of (a) 1C, (b) 2C, and (c) 3C.

a single phase consistent with $\text{PNb}_9\text{O}_{25}$ in the space group $I4/m$ with $a = 15.62054(7) \text{ \AA}$, $c = 3.82920(7) \text{ \AA}$, and unit cell volume of $934.33(2) \text{ \AA}^3$. These peaks were in a good agreement with previous studies [15].

Fig. 1(b) shows the cyclic voltammograms of the $\text{PNb}_9\text{O}_{25}$ half-cell at different scan rates between 1.0 V and 3.0 V vs. Li/Li^+ . It features four distinct pairs of cathodic and anodic peaks, revealing the reversibility of lithiation/delithiation in $\text{PNb}_9\text{O}_{25}$. In addition, all four pairs of redox peaks occurred at potential above 1.0 V vs. Li/Li^+ , confirming that $\text{PNb}_9\text{O}_{25}$ is a high voltage anode material for LIBs. The pair of cathodic and anodic peaks with the highest potential observed at

1.63/1.78 V vs. Li/Li^+ (blue dots), was attributed to $\text{Nb}^{5+}/\text{Nb}^{4+}$ redox reactions [15,45,46]. Likewise, the pair of cathodic and anodic peaks with the lowest potential observed at 1.12/1.28 V vs. Li/Li^+ (orange dots), was attributed to $\text{Nb}^{4+}/\text{Nb}^{3+}$ redox reactions [15,45,46]. The b-value associated with each cathodic and anodic peak was obtained by fitting the peak current I_{peak} vs. scan rate ν with a power law such that $I_{peak} = a\nu^b$ (see Supplementary Material). The b-values of these four cathodic and anodic peaks were around 0.6 suggesting that charging and discharging might be limited by diffusion of lithium in the $\text{PNb}_9\text{O}_{25}$ electrode [47]. Furthermore, two more pairs of cathodic and anodic peaks were observed at 1.37/1.45 V (red dots) and 1.49/1.56 V (green dots) vs. Li/Li^+ . The b-values associated with these peaks were found to be around 0.95 corresponding to fast and reversible redox reactions [47]. Such large b-values illustrate the potential of $\text{PNb}_9\text{O}_{25}$ anodes for high power density batteries despite undergoing phase transitions upon lithiation [47].

Fig. 1(c) shows galvanostatic charge and discharge profiles of $\text{PNb}_9\text{O}_{25}$ half-cell cycled between 1.0 and 3.0 V (vs. Li/Li^+) at different C-rates. At C-rate of C/10, the specific capacity was measured to be 225 mAh/g. The latter was larger than the theoretical capacity calculated as $C_{theo} = 190 \text{ mAh/g}$ based on the assumption of 1 electron per transition metal. Measurements by X-ray photoelectron spectroscopy showed that more than 1 electron was stored per transition metal confirming multi-electron redox reaction [12]. Two voltage plateaus were observed around 1.7 V and 1.1 V corresponding to the redox peaks with low b-values of 0.6 observed in Fig. 1(b).

Fig. 1(d) shows the specific capacity retention of the $\text{PNb}_9\text{O}_{25}$ electrode as a function of cycle number for C-rates ranging from C/10 to 40C. The capacity of the $\text{PNb}_9\text{O}_{25}$ electrode was around 200 mAh/g at C-rate of 1C. Furthermore, even at C-rate of 10 C, the $\text{PNb}_9\text{O}_{25}$ electrode showed impressive fast charging ability and maintained 75% of its capacity at C/10. In addition, after 30 cycles, it maintained its capacity and demonstrated excellent reversibility. By comparison, TiNb_2O_7 , one of the commercially accepted fast charging type lithium-ion battery anode materials, maintained 40% of its C/10 capacity at C-rate of 10 C [19].

4.2. Entropic potential of $\text{PNb}_9\text{O}_{25}$

Fig. 2 plots the open circuit voltage $U_{ocv}(x, T)$ and the entropic potential $\partial U_{ocv}(x, T)/\partial T$ at 20 °C as functions of x composition in $\text{Li}_x\text{PNb}_9\text{O}_{25}$ at C-rate of C/10 during lithiation. The trend of both measured $U_{ocv}(x, T)$ and $\partial U_{ocv}(x, T)/\partial T$ were repeatable during lithiation and subsequent delithiation at C-rate of C/10 (see Fig. S5 in Supplementary Material). It features six distinct regions based on the slope of $U_{ocv}(x, T)$ and $\partial U_{ocv}(x, T)/\partial T$. In Region I, corresponding to $x < 2$, both the open circuit voltage $U_{ocv}(x, T)$ and the entropic potential $\partial U_{ocv}(x, T)/\partial T$ feature sharp drop and sloped curve indicative of lithium insertion in a homogeneous solid solution [12,15]. Here, $\partial U_{ocv}(x, T)/\partial T$ decreased sharply upon lithiation in the homogeneous solid solution resulting in a more ordered structure. In Region II, for $2 \leq x \leq 3.5$, both $U_{ocv}(x, T)$ and $\partial U_{ocv}(x, T)/\partial T$ were constant and independent of x confirming a two-phase coexistence region also observed previously in XRD measurements [15]. Note that $U_{ocv}(x, T)$ associated with this two-phase coexistence region was 1.7 V (vs Li/Li^+) and corresponded to the potential of the redox peak observed in the CV curve [Fig. 1(a)]. In addition, *in situ* X-ray powder diffraction of $\text{PNb}_9\text{O}_{25}$ revealed that the structure goes through both solid solution regions and two-phase coexistence regions [12]. However, the two coexisting phases belong to the original refined space group with two different lattice parameters [12]. First, a solid solution of the original $I4/m$ space group was formed upon lithiation from $\text{PNb}_9\text{O}_{25}$ to $\text{Li}_2\text{PNb}_9\text{O}_{25}$. Second, between $\text{Li}_2\text{PNb}_9\text{O}_{25}$ and $\text{Li}_{3.5}\text{PNb}_9\text{O}_{25}$ the second $I4/m$ phase emerged with a larger unit cell volume confirming the two-phase coexistence region identified from the analysis of $U_{ocv}(x, T)$ and $\partial U_{ocv}(x, T)/\partial T$.

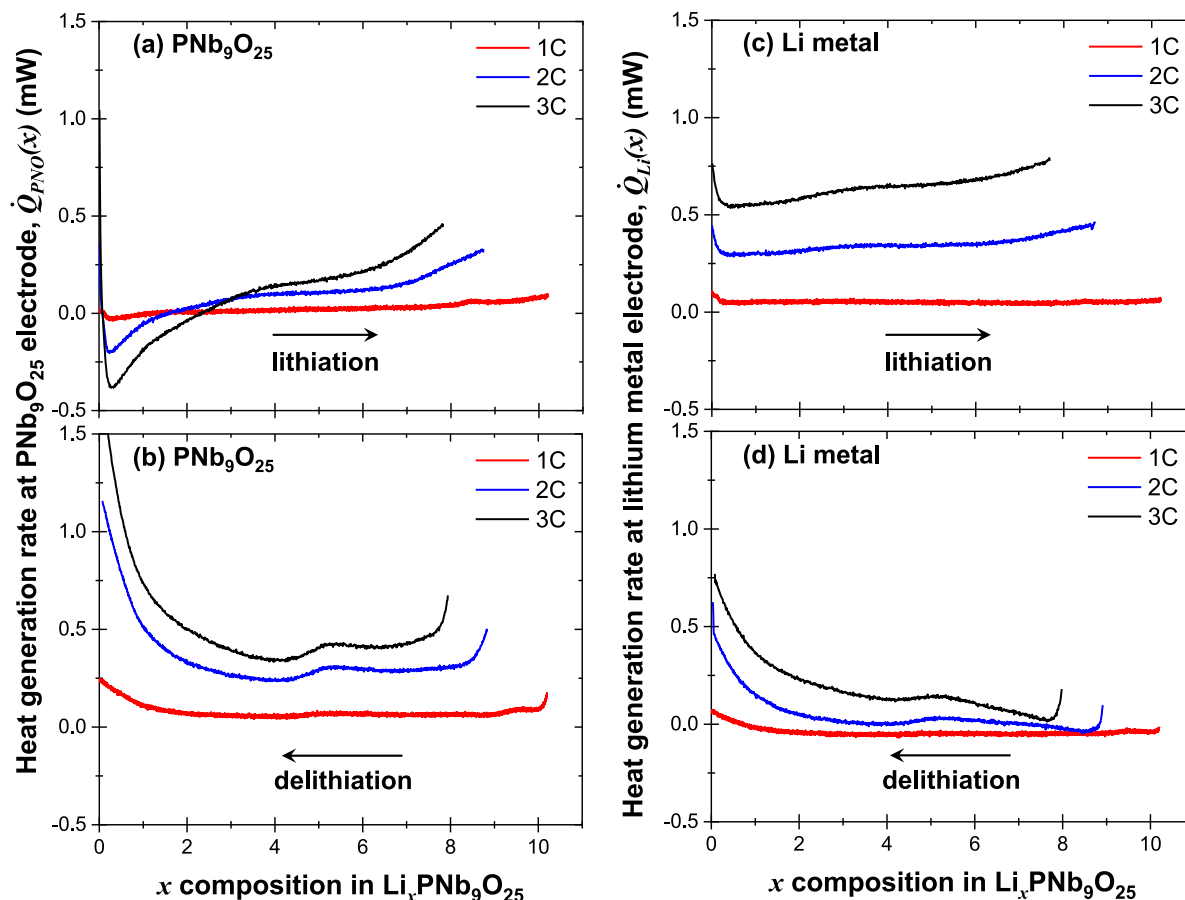


Fig. 4. Instantaneous heat generation rates $\dot{Q}_{PNO}(x)$ at the PNB₉O₂₅ electrode during (a) lithiation, (b) delithiation, and $\dot{Q}_{Li}(x)$ at the lithium metal electrode during (c) lithiation, (d) delithiation in the calorimetric cell cycled between 1.0 and 3.0 V vs. Li/Li⁺ at C-rates of 1C, 2C, and 3C as functions of x in Li_xPNb₉O₂₅.

For $3.5 \leq x \leq 9.5$, $U_{ocv}(x, T)$ shows a sloped potential suggesting a homogeneous solid solution. *In situ* XRD measurements also confirmed a monophasic lithiation process [45]. However, based on $\partial U_{ocv}(x, T)/\partial T$, this composition range can be further divided into three distinct regions. First, in Region III, defined by $3.5 \leq x \leq 5$, $\partial U_{ocv}(x, T)/\partial T$ increased first then decreased at higher x composition resulting in a local maxima. This behavior could be attributed to an semiconductor-to-metal transition known to occur in this region, based on magnetic susceptibility and solid-state nuclear magnetic resonance measurements, electrochemical impedance spectroscopy data, and density functional theory calculations [12]. The electronic entropy of insulating oxide is nearly zero due to the zero density of state at the Fermi level [48]. However, when the oxide becomes metallic, it exhibits high electronic entropy. Thus, $\partial U_{ocv}(x, T)/\partial T$, which corresponds essentially the partial molar entropy of the PNB₉O₂₅ electrode, featured a peak at the semiconductor-to-metal transition (see Supplementary Materials). In Region IV, such that $5 \leq x \leq 8$, $\partial U_{ocv}(x, T)/\partial T$ presents a small negative slope from -0.12 mV/K to -0.16 mV/K indicating the intercalation of lithium ion in a homogeneous solid solution. Furthermore, in Region V corresponding to $8 \leq x \leq 9.5$, $\partial U_{ocv}(x, T)/\partial T$ displays a tilde shape fluctuation. These observations were attributed to intralayer lithium ordering similar to that observed in TiS₂ [49] and LiCoO₂ [50]. Such ordering occurs when it is energetically advantageous for the intercalated lithium ions to arrange themselves in the vacant sites in a more ordered manner instead of being randomly inserted [17,19]. Furthermore, numerical simulations based on statistical mechanical modeling and validated experimentally with Li-ions in graphite suggest that the interatomic forces can cause ion ordering and result in tilde shape fluctuation in the partial molar entropy [51]. This intralayer lithium ordering possibly corresponds to fast lithium

transport within type- α edge sites with low kinetic barriers [12]. It is interesting to note that the XRD measurements suggest no crystallographic phase change in this region. Lastly, in Region VI with $x \geq 9.5$, both $U_{ocv}(x, T)$ and $\partial U_{ocv}(x, T)/\partial T$ were constant suggesting another two-phase coexistence of Li_{9.5}PNb₉O₂₅ and Li_{10.5}PNb₉O₂₅ phases.

Overall, the entropic potential measurements confirm the existence of two two-phase coexistence regions also identified from electrochemical testing and XRD measurements [12,15]. Most notably, the present analysis of both $U_{ocv}(x, T)$ and $\partial U_{ocv}(x, T)/\partial T$ also captured the entropic signature of semiconductor-to-metal transition (Region III) and intralayer ion ordering (region IV) which could not be identified from other characterization methods.

4.3. Heat generation rates

4.3.1. Instantaneous heat generation rates

Figs. 3(a)–3(c) plot the instantaneous heat generation rates $\dot{Q}_{PNO}(t)$ measured at the PNB₉O₂₅ electrode and $\dot{Q}_{Li}(t)$ at the lithium metal electrode as well as the total instantaneous heat generation rate $\dot{Q}_T(t) = \dot{Q}_{PNO}(t) + \dot{Q}_{Li}(t)$, as functions of dimensionless time t/t_{cd} , with t_{cd} being the charging/discharging cycle period, for three consecutive cycles at temperature of 20 °C and at C-rate of 1C, 2C, and 3C, respectively. First, the measurements at each electrode were repeatable cycle after cycle. In addition, the magnitude of $\dot{Q}_{Li}(t)$ at the lithium metal electrode was relatively constant over the charging or discharging step for any given C-rates unlike $\dot{Q}_{PNO}(t)$ at the PNB₉O₂₅ electrode which varied significantly with time.

Figs. 4(a) and 4(b) plot the instantaneous heat generation rates $\dot{Q}_{PNO}(x)$ measured at the PNB₉O₂₅ electrode during lithiation and delithiation at 20 °C as a function of composition x in Li_xPNb₉O₂₅ for

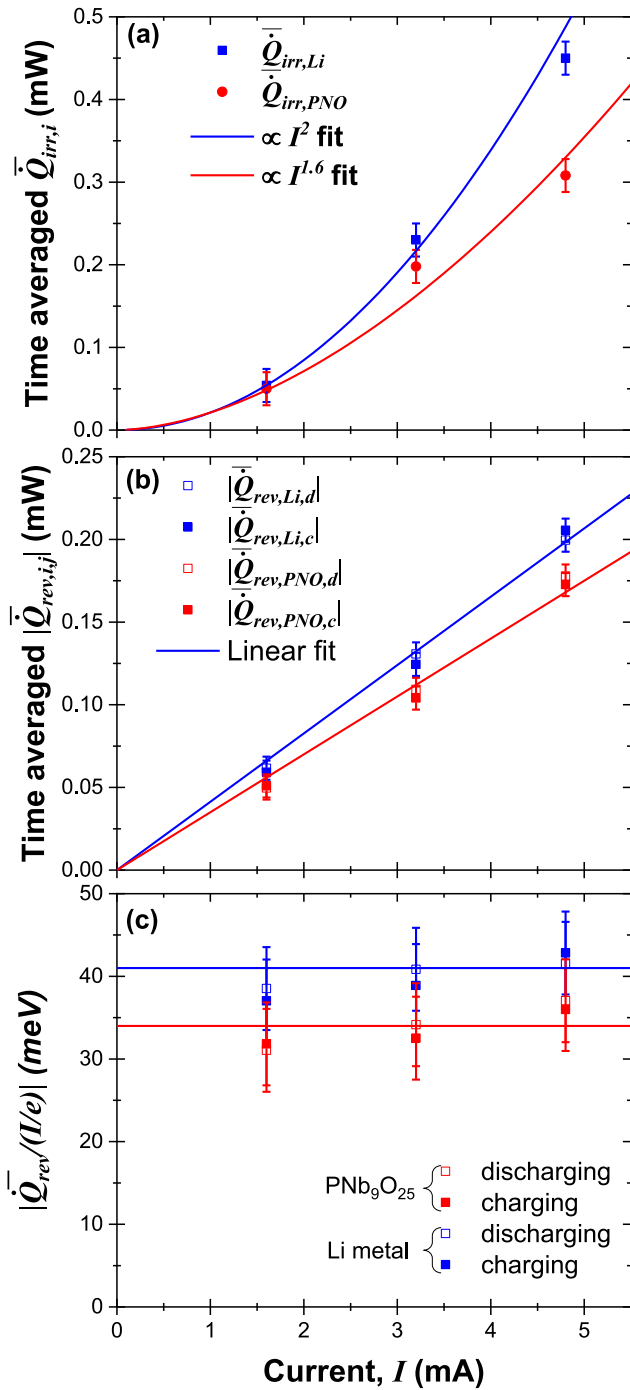


Fig. 5. Time-averaged (a) irreversible heat generation rates $\bar{Q}_{irr,PNO}$ and $\bar{Q}_{irr,Li}$, and (b) reversible heat generation rates $|\bar{Q}_{rev,PNO,j}|$ and $|\bar{Q}_{rev,Li,j}|$ during charging ($j = c$) and discharging ($j = d$), and (c) ratio of $|\bar{Q}_{rev,i,c}/(I/e)|$, as functions of current I , based on the isothermal operando calorimetry measurements at 20 °C.

C-rate of 1C, 2C, and 3C. At the onset of lithiation for $x \lesssim 2.0$, $\bar{Q}_{PNO}(x)$ featured an endothermic dip resulting in $\bar{Q}_{PNO}(x) \leq 0$. This can be attributed to the reversible entropic heat generation $\bar{Q}_{rev}(x)$ [Eq.(10)] characterized by a positive $\partial U_{ocv}(x, T)/\partial T$ and featuring a sharp drop as the lithium composition increased (Fig. 2). This dip was enhanced by the decrease in Joule heating $\bar{Q}_j(x) \geq 0$ due to the drop in electrical resistance of $\text{PNb}_9\text{O}_{25}$ associated with the insulator to semiconductor phase transition upon lithiation [12]. Indeed, the pristine $\text{PNb}_9\text{O}_{25}$ was white and electrically insulating but became black as it underwent

an insulator-to-semiconductor and semiconductor to metal transitions sequentially upon lithiation [12]. This transition was observed as a peak in the entropic potential measurements (Fig. 2). Beyond $x \simeq 2$, $\bar{Q}_{PNO}(x)$ was positive and increased with increasing C-rate due to the associated increase in Joule heating. Conversely, $\bar{Q}_{PNO}(x)$ increased sharply during delithiation at low lithium composition due to the exothermic reversible entropic heat generation and the increase in the electrical resistance of $\text{Li}_x\text{PNb}_9\text{O}_{25}$. Likewise, it also increased with increasing current or C-rate accompanied by the associated increase in Joule heating. In addition, Fig. 4(b) shows a local maxima for $x \simeq 5$ corresponding to the semiconductor-to-metal transition observed in the entropic potential $\partial U_{ocv}(x, T)/\partial T$ (Fig. 2).

Furthermore, Figs. 4(c) and 4(d) plot the instantaneous heat generation rate $\dot{Q}_{Li}(x)$ measured at the lithium metal electrode at 20 °C as a function of lithium composition x for C-rate ranging from 1C to 3C during lithiation and delithiation, respectively. Fig. 4(c) indicates that the magnitude of the heat generation rate at the lithium metal electrode $\dot{Q}_{Li}(x)$ was relatively constant throughout the lithiation process. This was attributed to the continuous Li^+ ion stripping and exothermic Li^+ ion solvation accompanied by ion-pairing in the EC:DMC electrolyte at constant current [52]. Then, $\dot{Q}_{Li}(x)$ increased with increasing current I . By contrast, Fig. 4(d) shows that $\dot{Q}_{Li}(x)$ increased during delithiation due to the plating of Li^+ on the lithium metal counter electrode accompanied by endothermic ion dissociation and exothermic dendrite formation on the surface of lithium metal counter electrode [53]. Indeed, during delithiation, Li^+ ions deintercalated from the $\text{PNb}_9\text{O}_{25}$ electrode, got solvated in EC:DMC and transported across the device until they reached the Li metal counter electrode where they lost their solvation shells before being deposited on the lithium metal electrode surface in the form of dendrites [54].

4.3.2. Time-averaged heat generation rates

Fig. 5(a) plots the time-averaged irreversible heat generation rates $\bar{Q}_{irr,PNO}$ and $\bar{Q}_{irr,Li}$ over a cycle at the $\text{PNb}_9\text{O}_{25}$ and the lithium metal electrodes as functions of imposed current I . Here, the square data points correspond to the time averaged $\bar{Q}_{irr,j}$ performed over 5 consecutive cycles at give C-rate. In addition, the error bars correspond to two standard deviations or 95% confidence interval. Fitting of $\bar{Q}_{irr,Li}(I)$ at the lithium metal electrode indicates that it increased quadratically with respect to I , i.e., $\bar{Q}_{irr,Li}(I) \propto I^2$. In other words, the irreversible heat generation was dominated by Joule heating as the electrode resistance of the Li electrode was constant and independent of the state of charge. In addition, $\bar{Q}_{irr,PNO}$ at the $\text{PNb}_9\text{O}_{25}$ electrode was similar to that of the lithium metal electrode $\bar{Q}_{irr,Li}$ at low current. However, $\bar{Q}_{irr,PNO}$ was smaller than $\bar{Q}_{irr,Li}$ at higher current. This can also be attributed to the increasing magnitude of the endothermic peak with increasing current (or C-rate) which resulted in negative $\bar{Q}_{PNO}(x)$ early in the lithiation process [Fig. 4(a)]. In addition, Joule heating in the $\text{PNb}_9\text{O}_{25}$ electrode did not vary as I^2 due to the important changes in its electrical resistivity upon lithium intercalation/deintercalation. Moreover, as the C-rate increased, the capacity of the battery decreased indicating that the amount of lithium intercalating/deintercalating also decreased. In fact, at C-rate of 1C, $\text{PNb}_9\text{O}_{25}$ was lithiated up to $\text{Li}_{10.5}\text{PNb}_9\text{O}_{25}$ while it was only lithiated up to $\text{Li}_8\text{PNb}_9\text{O}_{25}$ at C-rate of 3C for the same potential window. Thus, at high C-rate, the material underwent a narrower change in composition so that the average electrical resistivity also varied with C-rate.

Fig. 5(b) plots the time-averaged reversible heat generation rate $|\bar{Q}_{rev,PNO,j}|$ at the $\text{PNb}_9\text{O}_{25}$ working electrode and $|\bar{Q}_{rev,Li,j}|$ at the lithium metal counter electrode computed according to Eqs. (16)–(18) during lithiation ($j = d$) and delithiation ($j = c$) for different currents I . It establishes that both $|\bar{Q}_{rev,PNO,j}|$ and $|\bar{Q}_{rev,Li,j}|$ at each electrode were identical during lithiation and delithiation, confirming their reversible nature. Furthermore, both $|\bar{Q}_{rev,PNO,j}|$ and $|\bar{Q}_{rev,Li,j}|$ were linearly proportional to the current I . Combining Eqs. (7) and

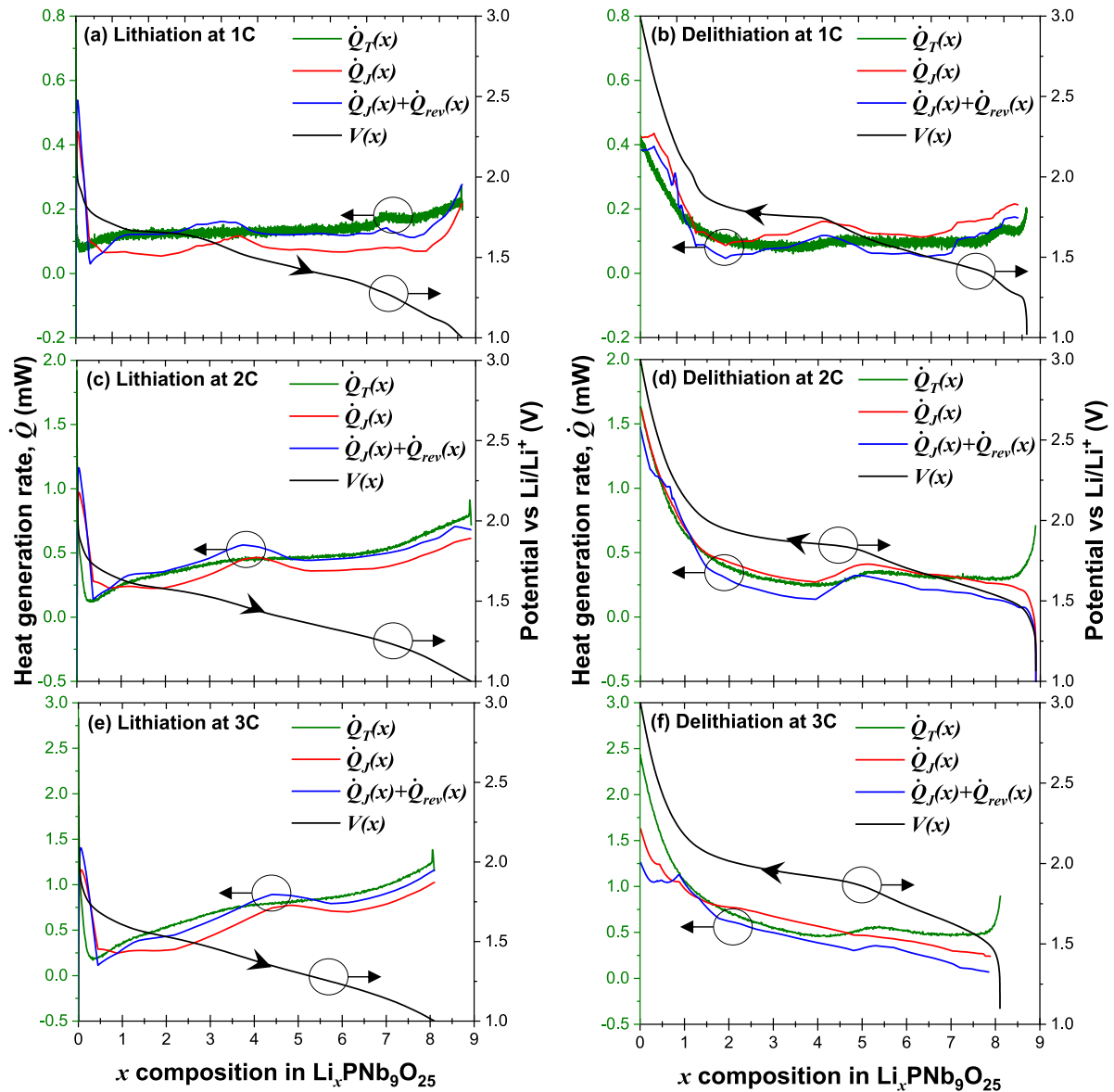


Fig. 6. Measured total heat generation rate $\dot{Q}_T(x)$ and heat generation rates $\dot{Q}_J(x)$, $\dot{Q}_J(x) + \dot{Q}_{rev}(x)$ calculated according to Eqs. (9) and (10) along with operating voltage $V(x)$ of a cell upon (a) lithiation, (b) delithiation at C-rate of 1C, (c) lithiation, (d) delithiation at C-rate of 2C, and (e) lithiation, (f) delithiation at C-rate of 3C at 20 °C.

(10) yields the time-averaged reversible heat generation rate $\bar{Q}_{rev,i}$ due to the entropic change at each electrode during galvanostatic cycling, i.e.,

$$\bar{Q}_{rev,Li} = -\frac{IT}{e} s_{Li}^o \quad \text{and} \quad \bar{Q}_{rev,PNO} = \frac{IT}{e} \frac{\partial \bar{s}_{PNO}}{\partial x}. \quad (20)$$

Thus, $\bar{Q}_{rev,Li}$ is exothermic (> 0) during discharging and endothermic (< 0) during charging whereas $\bar{Q}_{rev,PNO}$ is endothermic during discharging and exothermic during charging. In addition, Eq. (20) suggests that $\bar{Q}_{rev,i}$ is linearly proportional to current I in qualitative agreement with experimental data plotted in Fig. 5(b). The formation entropy s_{Li}^o of lithium metal is equal to 0.29 meV/K [55]. Based on the measured entropic potential $\partial U_{ocv}/\partial T$, the averaged $\partial \bar{s}_{PNO}/\partial x$ over all compositions x achieved during a cycle was estimated as 0.21 meV/K [Eq.(7)]. Thus, the ratio $|\bar{Q}_{rev,i,j}/(I/e)|$ should be equal to $T s_{Li}^o = 85$ meV for the lithium metal electrode and $T \partial \bar{s}_{PNO}/\partial x = 63$ meV for the $\text{PNb}_9\text{O}_{25}$ electrode at 20 °C [Eq.(20)]. Fig. 5(c) plots $|\bar{Q}_{rev,PNO,j}/(I/e)|$ vs. current I at the $\text{PNb}_9\text{O}_{25}$ ($i = \text{PNO}$) and at the Li metal ($i = \text{Li}$) electrode. It establishes that the ratios $|\bar{Q}_{rev,PNO,c/d}/(I/e)|$ and $|\bar{Q}_{rev,Li,c/d}/(I/e)|$ were independent of I for both lithiation and delithiation. Furthermore,

$|\bar{Q}_{rev,Li,c/d}/(I/e)|$ was larger than $|\bar{Q}_{rev,PNO,c/d}/(I/e)|$ as predicted from the entropic potential measurements. Here, $|\bar{Q}_{rev,Li,c/d}/(I/e)|$ was measured to be 41 meV while $|\bar{Q}_{rev,PNO,c/d}/(I/e)|$ was 34 meV. These values were smaller than the calculated $T s_{Li}^o$ and $T \partial \bar{s}_{PNO}/\partial x$, thus implying the occurrence of other physicochemical phenomena contributing to the reversible heat generation rate at each electrode.

The reversible heat generation rate at each electrode could be attributed not only to the entropic change [Eq.(10)] [22–24] but also to ion solvation/desolvation accompanied with ion-pairing [52,56–59], and to ion adsorption/desorption at the electrode surface [40,42–44]. Solvation or desolvation of Li^+ ions in carbonate takes place alternatively at the anode and cathode during charging and discharging. Thermochemistry calculations revealed that the enthalpy of solvation ΔH_{sol} of Li^+ ion in EC:DMC is negative so that the complexation of the Li^+ ion-carbonate is spontaneous and exothermic [56–58]. Conversely, desolvation is endothermic. Moreover, upon solvation, the solvated Li^+ ions may form ion-pairs with solvated PF_6^- [59]. The electric energy is released when two oppositely charged ions are brought together so that forming an ion pair is an exothermic process, i.e., $\Delta H_{el} < 0$ [52]. The enthalpy associated with ion-pairing ΔH_{ip} is the sum of the change

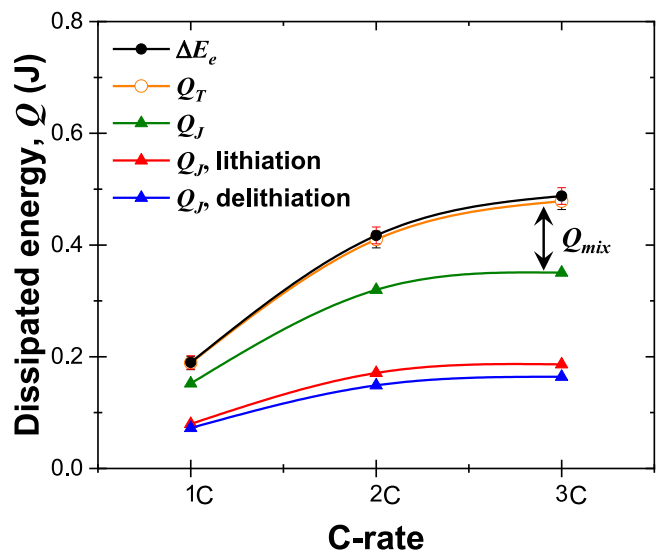


Fig. 7. Net electrical energy losses ΔE_e and total thermal energy dissipated Q_T averaged over the first five charging–discharging cycles as well as contributions from Joule heating Q_J during lithiation and delithiation. The enthalpy of mixing corresponds to $Q_{mix} = Q_T - Q_J = \Delta E_e - Q_J$.

in electric enthalpy ΔH_{el} due to ion association and the enthalpy of desolvation ΔH_{desol} , i.e., $\Delta H_{ip} = \Delta H_{el} + \Delta H_{desol} = \Delta H_{el} - \Delta H_{sol}$ [52]. More specifically, ΔH_{ip} for 1M of LiPF_6 in 1:1 v/v EC:DMC electrolyte was estimated using molecular dynamic simulations to be -0.8 kJ/mol at 20°C [52]. Thus, forming an ion-pairs is an exothermic process while dissociation of ion-pairs is endothermic. During charging, ion-pairing takes place at the $\text{PNb}_9\text{O}_{25}$ electrode while the reverse process occurs at the lithium metal counter electrode.

Finally, ion adsorption and desorption may also contribute to the reversible heat generation rate in battery electrodes. The heat generation rate associated with ion adsorption and desorption was found to be significant in electric double layer capacitor and was also proportional to the applied current I [40,42–44]. During charging, PF_6^- adsorbed to the $\text{PNb}_9\text{O}_{25}$ electrode while, simultaneously, Li^+ desorbed from it. Previous numerical simulations have established that the reversible heat generation rate decreased with increasing ion diameter [60]. Thus, the endothermic contribution of Li^+ desorption is more significant than the exothermic contribution of PF_6^- adsorption. In brief, reversible heat generation rates due to ion adsorption/desorption have opposite sign compared with those associated with reversible entropic change. Overall, calorimetric measurements established that the reversible heat generation rate at each electrode was dominated by the entropic changes with some contributions from ion solvation/desolvation accompanied with ion-pairing as well as ion adsorption/desorption.

4.3.3. Heat generation rate of a full cell

Figs. 6(a)–6(f) plot the total instantaneous heat generation rate $\dot{Q}_T(x) = \dot{Q}_{PNO}(x) + \dot{Q}_{Li}(x)$ as a functions of x in $\text{Li}_x\text{PNb}_9\text{O}_{25}$ measured in the entire cell at 20°C during lithiation and delithiation for C-rate of 1C, 2C, and 3C. It also shows the contributions from Joule heating $\dot{Q}_J(x)$ and entropic reversible heat generation $\dot{Q}_{rev}(x)$, respectively calculated using Eqs. (9) and (10) based on the measured open circuit voltage $U_{ocv}(x)$, operating voltage $V(x)$, and entropic potential $\partial U_{ocv}(x)/\partial T$ of the device. Here, for all C-rates considered, $\dot{Q}_J(x)$ decreased sharply for $x < 2$ during lithiation due to the transition of $\text{PNb}_9\text{O}_{25}$ from insulator to semiconductor upon lithiation. Conversely, $\dot{Q}_J(x)$ increased sharply for $x < 2$ during delithiation. It is interesting to note that the trends of the calculated Joule heating $\dot{Q}_J(x)$ was similar to those observed in the reported resistivity of the $\text{PNb}_9\text{O}_{25}$

electrode based on the electrochemical impedance spectroscopy measurements [12]. Moreover, predictions of the sum $\dot{Q}_J(x) + \dot{Q}_{rev}(x)$ agreed relatively well with the measured total heat generation rate $\dot{Q}_T(x)$ for both lithiation and delithiation. neglecting the heat generation rate due to side reactions $\dot{Q}_{sr}(x)$ leads to expressing the enthalpy of mixing $\dot{Q}_{mix}(x)$ as the difference between $\dot{Q}_T(x)$ and the sum $\dot{Q}_J(x) + \dot{Q}_{rev}(x)$, i.e., $\dot{Q}_{mix}(x) = \dot{Q}_T(x) - \dot{Q}_J(x) - \dot{Q}_{rev}(x)$ [Eq.(8)] [22–24]. Then, Fig. 6 indicates that $\dot{Q}_{mix}(x)$ increased with increasing C-rate. This can be attributed to larger Li^+ concentration gradients developed within the electrode due to diffusion limitation as the imposed current I increased [32].

4.3.4. Energy balance

Fig. 7 presents the electrical energy losses ΔE_e measured from the hysteresis in the cell potential $V(x, T)$ [Eq.(14)] at C-rates of 1C, 2C, and 3C. It also plots the measured total thermal energy Q_T dissipated in the entire cell along with the contributions from Joule heating Q_J [Eq.(13)] during lithiation and delithiation. Fig. 7 indicates that ΔE_e increased with increasing C-rates due to the associated increase in the overpotential $[V(x, T) - U^{avg}(x, T)]$ [28,29]. The values $U^{avg}(x, T)$ and $\partial U^{avg}(x, T)/\partial T$ measured by GITT at different C-rates used in the calculation of $\dot{Q}_J(x, T)$ and $\dot{Q}_{rev}(x, T)$ are shown in Figures S5–S6 of the Supplementary Material. Furthermore, the electrical energy losses ΔE_e fell within 4% of the measured total thermal energy Q_T dissipated over a cycle. In other words, the electrical energy losses were dissipated in the form of heat and the electrochemical measurements were in excellent agreement with the calorimetric measurements so that $\Delta E_e = Q_T$. Additionally, the irreversible Joule heating during delithiation was smaller than that during lithiation due to relatively fast kinetics of delithiation compared to that of lithiation, as observed in the apparent diffusion coefficient of Li^+ ion in the $\text{PNb}_9\text{O}_{25}$ electrode (see Supplementary Material).

Moreover, since $Q_{rev} \approx 0$, the difference between Q_T and Q_J corresponded to the heat dissipated as enthalpy of mixing, i.e., $Q_{mix} = Q_T - Q_J$. At C-rate of 1C, the irreversible Joule heating was responsible for 89% of the total energy dissipated while the enthalpy of mixing contributed only 11%. However, the contribution of the enthalpy of mixing to the total energy dissipated increased with increasing C-rate to reach 33% at C-rate of 3C. The present results suggest that the contribution of the enthalpy of mixing in the heat generation of $\text{PNb}_9\text{O}_{25}$ was relatively small compared with other battery electrode materials even at high C-rate [25]. These new results confirm that $\text{PNb}_9\text{O}_{25}$ is a very promising anode material for fast charging LIB applications.

5. Conclusion

This study investigated the charging mechanisms responsible for the fast charging of $\text{PNb}_9\text{O}_{25}$ electrode in lithium ion batteries. The cyclic voltammetry and galvanostatic cycling confirmed the impressive rate performance of $\text{PNb}_9\text{O}_{25}$ with cathodic and anodic peaks above 1 V (vs. Li/Li^+) thus avoiding SEI formation. Entropy measurements not only confirmed the phase transitions identified from XRD measurements but also identified semiconductor-to-metal transition and intralayer lithium ordering which could not be identified from other characterization methods. Moreover, this study reports, for the first time, the individual heat generation rates at the $\text{PNb}_9\text{O}_{25}$ working electrode and at the Li metal counter electrode in a battery cell during cycling. The heat generation rate due to Joule heating dominated the energy losses. The time-averaged irreversible heat generation rate indicated that the electrical resistance of the lithium metal electrode was constant and independent of the state of charge while the electrical resistance of the $\text{PNb}_9\text{O}_{25}$ changed significantly with the state of charge. Furthermore, the time-averaged reversible heat generation rates over the charging or discharging steps were equal and linearly proportional to the imposed current at both electrodes. In addition, entropic changes dominated

the reversible heat generation rate at each electrode. The enthalpy of mixing increased with the increasing C-rate but remained relatively small even at high C-rates compared to other LIB electrode materials. These results establish that $\text{PNb}_9\text{O}_{25}$ constitutes an excellent anode material undergoing insulator-to-metal transition and intralayer ion ordering during lithiation, two attractive features of fast charging battery applications.

CRedit authorship contribution statement

Sun Woong Baek: Conceptualization, Investigation, Formal analysis, Data curation, Visualization, Writing – original draft, Writing – review & editing. **Molleigh B. Preefer:** Conceptualization, Investigation, Visualization, Writing – original draft, Writing – review & editing. **Muna Saber:** Investigation, Formal analysis. **Kuan Zhai:** Investigation. **Matevž Frajnkovič:** Conceptualization. **Yucheng Zhou:** Investigation. **Bruce S. Dunn:** Supervision, Conceptualization. **Anton Van der Ven:** Supervision, Conceptualization. **Ram Seshadri:** Supervision, Conceptualization. **Laurent Pilon:** Supervision, Conceptualization, Project administration, Writing – review & editing.

Declaration of competing interest

The authors declare that they have no known competing financial interests or personal relationships that could have appeared to influence the work reported in this paper.

Acknowledgments

This work was supported as part of the Center for Synthetic Control Across Length-scales for Advancing Rechargeables (SCALAR), United States, an Energy Frontier Research Center funded by the U.S. Department of Energy, Office of Science, Basic Energy Sciences under Award # DE-SC0019381. The MRL Shared Experimental Facilities are supported by the MRSEC Program of the NSF, United States under Award No. DMR 1720256; a member of the NSF-funded Materials Research Facilities Network (www.mrfn.org).

Appendix A. Supplementary data

Supplementary material related to this article can be found online at <https://doi.org/10.1016/j.jpowsour.2021.230776>.

References

- [1] J.A. Rogers, Electronics for the human body, *JAMA* 313 (6) (2015) 561–562.
- [2] H. Guo, M.-H. Yeh, Y. Zi, Z. Wen, J. Chen, G. Liu, C. Hu, Z. Wang, Ultralight cut-paper-based self-charging power unit for self-powered portable electronic and medical systems, *ACS Nano* 11 (5) (2017) 4475–4482.
- [3] A. Meintz, J. Zhang, R. Vijayagopal, C. Kreuzer, S. Ahmed, I. Bloom, A. Burnham, R.B. Carlson, F. Dias, E.J. Dufek, Enabling fast charging–vehicle considerations, *J. Power Sources* 367 (2017) 216–227.
- [4] M. Walter, M.V. Kovalenko, K.V. Kravchyk, Challenges and benefits of post-lithium-ion batteries, *New J. Chem.* 44 (5) (2020) 1677–1683.
- [5] J.-T. Han, Y.-H. Huang, J.B. Goodenough, New anode framework for rechargeable lithium batteries, *Chem. Mater.* 23 (8) (2011) 2027–2029.
- [6] H. Liu, W. Li, D. Shen, D. Zhao, G. Wang, Graphitic carbon conformal coating of mesoporous TiO_2 hollow spheres for high-performance lithium ion battery anodes, *J. Am. Chem. Soc.* 137 (40) (2015) 13161–13166.
- [7] K.J. Griffith, A. Senyshyn, C.P. Grey, Structural stability from crystallographic shear in TiO_2 - Nb_2O_5 phases: Cation ordering and lithiation behavior of $\text{TiNb}_{24}\text{O}_{62}$, *Inorg. Chem.* 56 (7) (2017) 4002–4010.
- [8] C.P. Koçer, K.J. Griffith, C.P. Grey, A.J. Morris, Cation disorder and lithium insertion mechanism of wadsley-roth crystallographic shear phases from first principles, *J. Am. Chem. Soc.* 141 (38) (2019) 15121–15134.
- [9] B. Guo, X. Yu, X.-G. Sun, M. Chi, Z.-A. Qiao, J. Liu, Y.-S. Hu, X.-Q. Yang, J.B. Goodenough, S. Dai, A long-life lithium-ion battery with a highly porous TiNb_2O_7 anode for large-scale electrical energy storage, *Energy Environ. Sci.* 7 (2014) 2220–2226.
- [10] R.S. Roth, A.D. Wadsley, S. Andersson, The crystal structure of $\text{PNb}_9\text{O}_{25}$, *Acta Crystallogr.* 18 (4) (1965) 643–647.
- [11] X. Zhu, J. Xu, Y. Luo, Q. Fu, G. Liang, L. Luo, Y. Chen, C. Lin, X.S. Zhao, $\text{MoNb}_{12}\text{O}_{33}$ as a new anode material for high-capacity, safe, rapid and durable Li^+ storage: structural characteristics, electrochemical properties and working mechanisms, *J. Mater. Chem. A* 7 (2019) 6522–6532.
- [12] M.B. Preefer, M. Saber, Q. Wei, N.H. Bashian, J.D. Bocarsly, W. Zhang, G. Lee, J. Milam-Guerrero, E.S. Howard, R.C. Vincent, B.C. Melot, A. Van der Ven, R. Seshadri, B.S. Dunn, Multielectron redox and insulator-to-metal transition upon lithium insertion in the fast-charging, Wadsley-Roth phase $\text{PNb}_9\text{O}_{25}$, *Chem. Mater.* 32 (11) (2020) 4553–4563.
- [13] H. Yu, J. Zhang, M. Xia, C. Deng, X. Zhang, R. Zheng, S. Chen, J. Shu, Z.-B. Wang, $\text{PNb}_9\text{O}_{25}$ nanofiber as a high-voltage anode material for advanced lithium ions batteries, *J. Materiomics* 6 (4) (2020) 781–787.
- [14] H. Yu, J. Zhang, R. Zheng, T. Liu, N. Peng, Y. Yuan, Y. Liu, J. Shu, Z.-B. Wang, The journey of lithium ions in the lattice of $\text{PNb}_9\text{O}_{25}$, *Mater. Chem. Front.* 4 (2020) 631–637.
- [15] S. Patoux, M. Dolle, G. Rousse, C. Masquelier, A reversible lithium intercalation process in an ReO_3 type structure $\text{PNb}_9\text{O}_{25}$, *J. Electrochem. Soc.* 149 (4) (2002) A391–A400.
- [16] J. Schmidt, A. Weber, E. Ivers-Tiffée, A novel and precise measuring method for the entropy of lithium-ion cells: δS via electrothermal impedance spectroscopy, *Electrochim. Acta* 137 (2014) 311–319.
- [17] N.S. Hudak, L.E. Davis, G. Nagasubramanian, Cycling-induced changes in the entropy profiles of lithium cobalt oxide electrodes, *J. Electrochem. Soc.* 162 (3) (2014) A315.
- [18] A. Van der Ven, J. Bhattacharya, A.A. Belak, Understanding Li diffusion in Li-intercalation compounds, *Acc. Chem. Res.* 46 (5) (2013) 1216–1225.
- [19] S.W. Baek, K.E. Wyckoff, D.M. Butts, J. Bienz, A. Likitchchawankun, M.B. Preefer, M. Frajnkovič, B.S. Dunn, R. Seshadri, L. Pilon, *Operando* Calorimetry informs the origin of rapid rate performance in microwave-prepared TiNb_2O_7 electrodes, *J. Power Sources* 490 (2021) 229537.
- [20] O. Munteshari, J. Lau, A. Krishnan, B.S. Dunn, L. Pilon, Isothermal calorimeter for measurements of time-dependent heat generation rate in individual supercapacitor electrodes, *J. Power Sources* 374 (2018) 257–268.
- [21] M.J. Moran, M.B. Bailey, D.D. Boettner, H.N. Shapiro, *Fundamentals of Engineering Thermodynamics*, John Wiley & Sons, New York, NY, 2018.
- [22] G. Liu, M. Ouyang, L. Lu, J. Li, X. Han, Analysis of the heat generation of lithium-ion battery during charging and discharging considering different influencing factors, *J. Therm. Anal. Calorim.* 116 (2) (2014) 1001–1010.
- [23] G. Assat, S.L. Glazier, C. Delacourt, J.-M. Tarascon, Probing the thermal effects of voltage hysteresis in anionic redox-based lithium-rich cathodes using isothermal calorimetry, *Nature Energy* 4 (8) (2019) 647–656.
- [24] J. Newman, K.E. Thomas, H. Hafezi, D.R. Wheeler, Modeling of lithium-ion batteries, *J. Power Sources* 119 (2003) 838–843.
- [25] K.E. Thomas, J. Newman, Thermal modeling of porous insertion electrodes, *J. Electrochem. Soc.* 150 (2) (2003) A176.
- [26] S. Ma, M. Jiang, P. Tao, C. Song, J. Wu, J. Wang, T. Deng, W. Shang, Temperature effect and thermal impact in lithium-ion batteries: A review, *Prog. Nat. Sci. Mater. Int.* 28 (6) (2018) 653–666.
- [27] T. Tsujikawa, K. Yabuta, T. Matsushita, T. Matsushima, K. Hayashi, M. Arakawa, Characteristics of lithium-ion battery with non-flammable electrolyte, *J. Power Sources* 189 (1) (2009) 429–434.
- [28] M. Ecker, J.B. Gerschler, J. Vogel, S. Käbitz, F. Hust, P. Dechent, D.U. Sauer, Development of a lifetime prediction model for lithium-ion batteries based on extended accelerated aging test data, *J. Power Sources* 215 (2012) 248–257.
- [29] D. Andre, M. Meiler, K. Steiner, C. Wimmer, T. Soczka-Guth, D.U. Sauer, Characterization of high-power lithium-ion batteries by electrochemical impedance spectroscopy. I. experimental investigation, *J. Power Sources* 196 (12) (2011) 5334–5341.
- [30] Y. Bai, L. Li, Y. Li, G. Chen, H. Zhao, Z. Wang, C. Wu, H. Ma, X. Wang, H. Cui, et al., Reversible and irreversible heat generation of NCA/Si-C pouch cell during electrochemical energy-storage process, *J. Energy Chem.* 29 (2019) 95–102.
- [31] W. Lu, J. Prakash, In situ measurements of heat generation in a Li/mesocarbon microbead half-cell, *J. Electrochem. Soc.* 150 (3) (2003) A262.
- [32] K. Thomas, J. Newman, Heats of mixing and of entropy in porous insertion electrodes, *J. Power Sources* 119 (2003) 844–849.
- [33] K. Smith, C.-Y. Wang, Power and thermal characterization of a lithium-ion battery pack for hybrid-electric vehicles, *J. Power Sources* 160 (1) (2006) 662–673.
- [34] Y. Wang, K. Zaghbi, A. Guerfi, F. Bazito, R. Torresi, J. Dahn, Accelerating rate calorimetry studies of the reactions between ionic liquids and charged lithium ion battery electrode materials, *Electrochim. Acta* 52 (22) (2007) 6346–6352.
- [35] X. Feng, M. Fang, X. He, M. Ouyang, L. Lu, H. Wang, M. Zhang, Thermal runaway features of large format prismatic lithium ion battery using extended volume accelerating rate calorimetry, *J. Power Sources* 255 (2014) 294–301.
- [36] H. Giel, D. Henriques, G. Bourne, T. Markus, Investigation of the heat generation of a commercial 2032 (LiCoO_2) coin cell with a novel differential scanning battery calorimeter, *J. Power Sources* 390 (2018) 116–126.

- [37] A. Du Pasquier, F. Disma, T. Bowmer, A. Gozdz, G. Amatucci, J.-M. Tarascon, Differential scanning calorimetry study of the reactivity of carbon anodes in plastic Li-ion batteries, *J. Electrochem. Soc.* 145 (2) (1998) 472–477.
- [38] Y. Saito, K. Kanari, K. Takano, Thermal studies of a lithium-ion battery, *J. Power Sources* 68 (2) (1997) 451–454.
- [39] O. Munteshari, J. Lau, D.S. Ashby, B.S. Dunn, L. Pilon, Effects of constituent materials on heat generation in individual EDLC electrodes, *J. Electrochem. Soc.* 165 (7) (2018) A1547.
- [40] A. Likitchatchawankun, A. Kundu, O. Munteshari, T.S. Fisher, L. Pilon, Heat generation in all-solid-state supercapacitors with graphene electrodes and gel electrolytes, *Electrochim. Acta* 303 (2019) 341–353.
- [41] A. Likitchatchawankun, R.H. DeBlock, G. Whang, O. Munteshari, M. Frajnkovič, B.S. Dunn, L. Pilon, Heat generation in electric double layer capacitors with neat and diluted ionic liquid electrolytes under large potential window between 5 and 80°C, *J. Power Sources* 488 (2021) 229368.
- [42] A. Likitchatchawankun, G. Whang, J. Lau, O. Munteshari, B.S. Dunn, L. Pilon, Effect of temperature on irreversible and reversible heat generation rates in ionic liquid-based electric double layer capacitors, *Electrochim. Acta* 338 (2020) 135802.
- [43] O. Munteshari, J. Lau, A. Likitchatchawankun, B.-A. Mei, C.S. Choi, D. Butts, B.S. Dunn, L. Pilon, Thermal signature of ion intercalation and surface redox reactions mechanisms in model pseudocapacitive electrodes, *Electrochim. Acta* 307 (2019) 512–524.
- [44] O. Munteshari, A. Borenstein, R.H. DeBlock, J. Lau, G. Whang, Y. Zhou, A. Likitchatchawankun, R.B. Kaner, B.S. Dunn, L. Pilon, In operando calorimetric measurements for activated carbon electrodes in ionic liquid electrolytes under large potential windows, *ChemSusChem* 13 (5) (2020) 1013–1026.
- [45] H. Yu, J. Zhang, R. Zheng, T. Liu, N. Peng, Y. Yuan, Y. Liu, J. Shu, Z.-B. Wang, The journey of lithium ions in the lattice of $\text{PNb}_9\text{O}_{25}$, *Mater. Chem. Front.* 4 (2) (2020) 631–637.
- [46] H. Yu, J. Zhang, M. Xia, C. Deng, X. Zhang, R. Zheng, S. Chen, J. Shu, Z.-B. Wang, $\text{PNb}_9\text{O}_{25}$ nanofiber as a high-voltage anode material for advanced lithium ions batteries, *J. Materiomics* 6 (4) (2020) 781–787.
- [47] T. Kim, W. Choi, H.-C. Shin, J.-Y. Choi, J. Kim, M.-S. Park, W.-S. Yoon, Applications of voltammetry in lithium ion battery research, *J. Electrochem. Sci. Technol.* 11 (1) (2020) 14–25.
- [48] F. Zhou, T. Maxisch, G. Ceder, Configurational electronic entropy and the phase diagram of mixed-valence oxides: the case of Li_xFePO_4 , *Phys. Rev. Lett.* 97 (15) (2006) 155704.
- [49] J. Dahn, R.R. Haering, Lithium intercalation in TiS_2 , *Mater. Res. Bull.* 14 (10) (1979) 1259–1262.
- [50] Y. Reynier, J. Graetz, T. Swan-Wood, P. Rez, R. Yazami, B. Fultz, Entropy of Li intercalation in Li_xCoO_2 , *Phys. Rev. B* 70 (17) (2004) 174304.
- [51] M. Otero, A. Sigal, E.M. Perassi, D. Barraco, E.P.M. Leiva, Statistical mechanical modeling of the transition stage II \rightarrow stage I of Li-ion storage in graphite. A priori vs induced heterogeneity, *Electrochim. Acta* 245 (2017) 569–574.
- [52] C.L. Berhaut, D. Lemordant, P. Porion, L. Timperman, G. Schmidt, M. Anouti, Ionic association analysis of LiTDI, LiFSI and LiPF₆ in EC/DMC for better Li-ion battery performances, *RSC Adv.* 9 (8) (2019) 4599–4608.
- [53] U. Janakiraman, T.R. Garrick, M.E. Fortier, Lithium plating detection methods in Li-ion batteries, *J. Electrochem. Soc.* 167 (16) (2020) 160552.
- [54] F. Hao, A. Verma, P.P. Mukherjee, Mechanistic insight into dendrite-SEI interactions for lithium metal electrodes, *J. Mater. Chem. A* 6 (40) (2018) 19664–19671.
- [55] M.W. Chase Jr., Nist-janaf thermochemical tables, *J. Phys. Chem. Ref. Data, Monogr.* 9 (1998).
- [56] M. Shakourian-Fard, G. Kamath, S.K. Sankaranarayanan, Evaluating the free energies of solvation and electronic structures of lithium-ion battery electrolytes, *ChemPhysChem* 17 (18) (2016) 2916–2930.
- [57] W. Cui, Y. Lansac, H. Lee, S.-T. Hong, Y.H. Jang, Lithium ion solvation by ethylene carbonates in lithium-ion battery electrolytes, revisited by density functional theory with the hybrid solvation model and free energy correction in solution, *Phys. Chem. Chem. Phys.* 18 (34) (2016) 23607–23612.
- [58] O. Borodin, M. Olguin, P. Ganesh, P.R. Kent, J.L. Allen, W.A. Henderson, Competitive lithium solvation of linear and cyclic carbonates from quantum chemistry, *Phys. Chem. Chem. Phys.* 18 (1) (2016) 164–175.
- [59] D.M. Seo, S. Reiningger, M. Kutcher, K. Redmond, W.B. Euler, B.L. Lucht, Role of mixed solvation and ion pairing in the solution structure of lithium ion battery electrolytes, *J. Phys. Chem. C* 119 (25) (2015) 14038–14046.
- [60] A.L. d'Entremont, L. Pilon, Thermal effects of asymmetric electrolytes in electric double layer capacitors, *J. Power Sources* 273 (2015) 196–209.